
# Rheological effects of a gas fluidized bed emulsion on falling and rising spheres



Citation for the original published paper (version of record):
Köhler, A., Guío-Pérez, D., Prati, A. et al (2021). Rheological effects of a gas fluidized bed emulsion on falling and rising spheres. Powder Technology, 393: 510-518.
http://dx.doi.org/10.1016/j.powtec.2021.07.064

Powder Technology 393 (2021) 510–518

Contents lists available at ScienceDirect

Powder Technology

journal homepage: www.elsevier.com/locate/powtec

# Rheological effects of a gas fluidized bed emulsion on falling and rising spheres

Anna Köhler [a,*], Diana Carolina Guío-Pérez [a], Anna Prati [b], Michele Larcher [b], David Pallarès [a]

[a] Dept. of Space, Earth and Environment, Chalmers University of Technology, 41296 Gothenburg, Sweden
[b] Faculty of Science and Technology, Free University of Bozen-Bolzano, Bolzano 39100, Italy

ARTICLE INFO

*Article history:*
Received 30 December 2020
Received in revised form 6 May 2021
Accepted 21 July 2021
Available online 24 July 2021

*Keywords:*
Gas-solid fluidization
Minimum fluidization
Falling/rising spheres
Magnetic particle tracking
Viscoplastic rheology
Yield stress

ABSTRACT

To enable the mechanistic description of the mixing of larger particles in gas-fluidized beds in models (e.g. fuel particles in combustors), knowledge about the rheology of the bed emulsion is required. Here, it is crucial to determine the drag on large fuel-alike particles.

This work presents the experimental work on the fate of 13 different solid spheres falling or rising through a bed of air and glass beads at minimum fluidization. The trajectories of the tracer are highly resolved (sampling rate of 200 Hz) by means of magnetic particle tracking, this previously unmet accuracy allows disclosing the complex rheological behavior of gas-solids fluidized bed emulsions in terms of drag on immersed objects. The trajectories reveal that none of the tracers reach terminal velocity during their fall and rise through the bed. The shear stress is obtained through the drag force by solving the equation of motion for the tracer. The data reveal particularities of the bed rheology and clear differences of its effect on rising and falling particles. When studying the shear stress over the characteristic shear rate of each tracer, it can be seen that the stress of the bed on the tracers is dominated by a yield stress, with a somewhat smaller contribution of the shear stress. For rising tracers this last contribution is almost negligible.

The falling tracers show strong interaction with the bed emulsion, resulting in a fluctuating shear stress, which increases with tracer size and density. The stagnation of some tracers at low shear rates reveals a viscoplastic behavior of the bed emulsion, exhibiting a typical yield stress that showing a clear dependence on the tracer diameter and buoyant density. The concept of yield gravity is used in order to introduce a normalized shear stress which provides additional verification of the experimental observations in relation to the influence of tracer size and relative density on the shear stress.



## 1. Introduction

Fluidization is the dynamic fluid-like state developed when a gas or liquid flows with a sufficiently high velocity through a bed of particulate solids. The lifted solids form an emulsion phase with the fluidizing agent and have in this mobile state, an enhanced availability to be transported and to participate in reactive processes and heat transfer. This mobility makes the fluidization phenomena a widely spread technology with applications ranging from the synthesis industry to the energy sector, where fluidized bed (FB) reactors are mainly used for solid fuel conversion.

Just like fluids are given general physical properties such as density, viscosity and surface tension, it is desirable to derive such properties for a fluidized bed, for them to be included in mathematical models and be used for the design of reactive units. A dense bed can generally be divided into two phases: the emulsion phase, which is considered to remain at minimum fluidization, and the bubble phase, consisting of the excess gas (with respect to the minimum fluidization volume flow) that flows in form of rising bubbles. While the emulsion density is rather easily obtained at minimum fluidization velocity with the pressure over the bed, obtaining the viscosity (a critical property for the mixing of large objects immersed in the bed, (e.g. fuel particles in boilers and gasifiers), remains a difficult and lively discussion in literature.

As early as in 1906, Einstein formulated the apparent viscosity of very dilute suspensions (particle volume fraction, $\phi < 0.03$) as function of the solids concentration based on a Newtonian approach [1]. The concept has been taken up and further developed by many authors, e.g. [2–4], foremost to include hydrodynamic particle-particle interactions, dominant in denser suspensions ($\phi < 0.4$). The theory was introduced into the field of liquid fluidization, where particle concentrations reach up to $\phi < 0.6$, by Poletto and Joseph [5], as well as, by the extensive work of Di Felice and colleagues [6–8].

* Corresponding author.
*E-mail address:* anna.koehler@bioshare.se (A. Köhler).

https://doi.org/10.1016/j.powtec.2021.07.064

Still, due to the intrinsic flow instability of gas FBs beyond minimum fluidization velocity, the above named models fail to predict the apparent viscosity of gas fluidized systems [8]. Instead, experimental measures were early exploit to determine the viscosity of gas fluidized beds: Daniels [9], followed by others, [10,11], used the terminal velocity of falling spheres in the laminar regime to determine the apparent viscosity of different gas-fluidized materials at minimum fluidization, concluding that the bed emulsion behaves like a Newtonian fluid in terms of drag force on immersed objects. However, their analyses were based on measurements with a strongly limited spatial resolution in which the falling tracers where assumed to keep a constant average velocity derived from the time and distance between two detection heights. In a later study, applying a known constant upwards force on spherical tracer particles immersed in a gas-solids emulsion at minimum fluidization, Daniels [12] was not able to fit the Newtonian model [13] to their results. The observed behavior was later interpreted by Wei and Chen to be similar to that of Bingham plastics [14]. Still using Daniels [9] experimental data and assuming a defluidized zone above the moving object, Rees et al. [15] observed that the apparent viscosity of the bed emulsion followed a deviated Stokes' law, originally deduced for non-compressible Newtonian fluid. Their model results were in line with other data found in literature showing that the effective drag-related viscosity of the gas-solids emulsion on larger objects increases with the mean particle size of the bed material, for low Reynolds numbers. However, it must be noted that their assumption of the bed behaving like a Newtonian fluid and the derived values of the effective viscosity therefrom are all based on measurement data with strongly limited spatial resolution.

A common method to determine the intrinsic viscosity of a fluid is the use of a rotational viscometer, as done by Schügerl et al. [16] and others [17–20], which enables the measurements at different constant shear rates adjusted through the rotational velocity. Grace [21], who early reviewed the literature about viscosity in gas FBs, claimed that both the falling sphere and the rotational viscometer method alter the behavior of the bed emulsion and hence its viscosity. Instead, he evaluated the bed viscosity by measuring with X-ray the velocity of the rising bubbles formed in gas FBs. While the behavior of the FB rheology in terms of Newtonian or not could not be confirmed with this method, the author reasoned that given the shear-thickening behavior known from other solid suspensions and the local foreseeable variations in solids concentration around a moving object, a non-Newtonian rheology could be expected. This suspected non-Newtonian behavior was later on indicated by several authors [8,16,22,23] and experimentally evidenced in more recent studies in rotational viscometers [18,20], where shear-thinning was observed at high shear rates representative for common fluidized bed applications [20].

As suggested by literature [21], different values of the apparent viscosity should be expected from rotational viscometers (providing the intrinsic viscosity of the gas-solids emulsion governing the internal transfer of momentum) and the falling sphere method (providing the effective viscosity for the drag exerted by the gas-solids emulsion on an immersed object). For the latter, the presence of the immersed object will affect the fluidization and thus the local properties of the gas-solids emulsion, which in turn influences the shear stress acting on it.

In summary, previous research of the effective viscosity for the drag of gas-solids emulsion on immersed objects lacked the experimental spatial resolution needed to confirm or discard the expected non-Newtonian behavior of the gas-solids emulsion and was limited to the laminar flow regime. Further, studies in rotational viscometers indicate an intrinsic non-Newtonian behavior of the gas-solids emulsion, but are not applicable to determine the effective viscosity acting on immersed objects.

This work seeks to investigate the shear stress generated by the gas-solids emulsion on larger objects during their gravity-driven falling motion with slip velocities covering all flow regimes typical for FB operation. By means of magnetic particle tracking (MPT), previously developed by the authors [24], acceleration profiles can be obtained at high resolution (200 Hz). This high accuracy is here used to disclose the rheological properties and effective drag of the gas-solids emulsion on both falling and rising spherical tracers.

## 2. Theory

The drag force on a spherical object immersed in a fluidized bed is generally expressed as

$$F_D = C_D \pi \rho_{em} \frac{D_p^2}{4} \frac{|u_p - u_{em}|^2}{2} \tag{1}$$

where $C_D$ is the drag coefficient, $D_p$ the object diameter, $u_{em}$ the velocity of the emulsion, $u_p$ the velocity of the object, and $\rho_{em}$ the bulk density of fluidized bed emulsion. For a tracer moving vertically through the bed, the motion induces a vertical flow of the bed solids, which have to be lifted to make space for the downwards motion of the tracer particle. This velocity is obtained by the continuity equation over the cross-section of the bed, reading

$$u_{em} = \frac{D_p^2}{D_b^2 - D_p^2} u_p = \lambda u_p. \tag{2}$$

The bulk density at minimum fluidization can be obtained from the volume occupied by the gas-solids emulsion consisting of a given mass of bed material.

$$\rho_{em} = \varepsilon_{mf}\rho_g + (1-\varepsilon_{mf})\rho_s \approx \frac{m_b}{A_b L_{mf}} \tag{3}$$

where $\varepsilon_{mf}$ is the void fraction at minimum fluidization, $m_b$ is the mass of the bed material, $A_b$ is the cross-sectional area of the bed, and $L_{mf}$ is the height of the bed at minimum fluidization.

Further, the vertical component of the equation of motion for an immersed tracer reads

$$m_p \frac{du_z}{dt} = \sum F = F_G + F_B + F_D + F_V \tag{4}$$

where $m_p$ and $u_z$ are the mass and the vertical velocity of the object, respectively. Here, $F_G$ is the gravity term, $F_B$ is the buoyancy term, $F_D$ is the drag term and $F_V$ is the virtual mass term [25]. Wall effects influence the motion of the object as disclosed by several authors ([26,27] among others), but are expected to play a minor role for Reynolds numbers in the transient regime [28] and are therefore neglected in this work. Combining Eqs. (1), (2) and (3), and developing their terms, yields

$$\frac{\pi}{6} D_p^3 \rho_p \frac{du_z}{dt} = \frac{\pi}{6} D_p^3 \left(\rho_p - \rho_{em}\right) g + \frac{\pi}{8} D_p^2 C_D \rho_{em} (1-\lambda)^2 u_z^2 + \frac{\pi}{12} D_p^3 \rho_{em} \left( (1-\lambda) \frac{Du_z}{Dt} - \frac{du_z}{dt} \right) \tag{5}$$

where $\rho_p$ is the density of the immersed object and g is the intensity of gravity acceleration. With the gas-solids emulsion being compressible, the induced vertical flow of bed solids has an inherent complexity yielding fluctuating patterns and local variations. However, for simplicity the average velocity of the net vertical flow of the solids emulsion induced by the fall of the tracer is considered (cf. Eq. (2)). With the tracer trajectory experimentally resolved, the velocity and acceleration can be derived, and the drag coefficient can be obtained by solving Eq. (5) as

$$C_D = \frac{2}{3} \frac{D_p}{(1-\lambda)^2 u_z^2} \left( 2g \left( 1 - \frac{\rho_p}{\rho_{em}} \right) + \frac{du_z}{dt} \left( 2 \frac{\rho_p}{\rho_{em}} - (1-\lambda) \frac{Du_z}{Dt} + 1 \right) \right) \tag{6}$$

The shear stress, $\tau$, on the object is defined as the drag force over the surface area of the spherical object and can with Eq. (6) be written as

$$\tau = \frac{F_D}{A_s} = \frac{1}{8} C_D \rho_{em} (1-\lambda)^2 u_z^2$$
$$= \frac{1}{12} D_p \left( \underbrace{2g\left(\rho_{em} - \rho_p\right)}_{\text{buoyancy}} + \underbrace{2\frac{du_z}{dt}\rho_p}_{\text{acceleration}} + \underbrace{\rho_{em}\left(\frac{du_z}{dt} - (1-\lambda)\frac{Du_z}{Dt}\right)}_{\text{added mass}} \right) \quad (7)$$

Note, Andres [29] derived an alternative definition of the drag force using solely the vertical projection of the shear stress over the sphere surface. As this results in a slightly higher coefficient for spherical objects only (i.e. $\frac{2}{3\pi}$ instead of $\frac{1}{6}$), this work reports the shear stress averaged over the total surface area of the sphere. In reality, the local shear stress is likely to vary over the tracer surface: Tian et al. [30] conducted experiments with a granular driven particulate flow over a still hexagonal tube and found particles to stagnate in the area on top of the tube. In the case of falling spheres, this suggests bulk solids to stagnate below the spheres, thus, not contributing to the shear stress. However, as the bulk solids are fluidized and can rearrange freely, the effect of stagnant bulk solids is believed to be minor in a fluidized bed. Rees et al. [31] found the presence of a so-called "defluidized hood" above rising and falling spheres, a region with stagnant bulk solids, which moves with the particle. In a later work, the authors found that for falling tracers the upwards moving hood detaches from the particle, which suggests its influence on the shear stress to be neglectable.

The effective viscosity is defined as the ratio between the shear stress, $\tau$ and the shear rate, $\dot{\gamma}$, over the surface area of the object.

$$\tau = \mu_{eff}\, \dot{\gamma}\,. \quad (8)$$

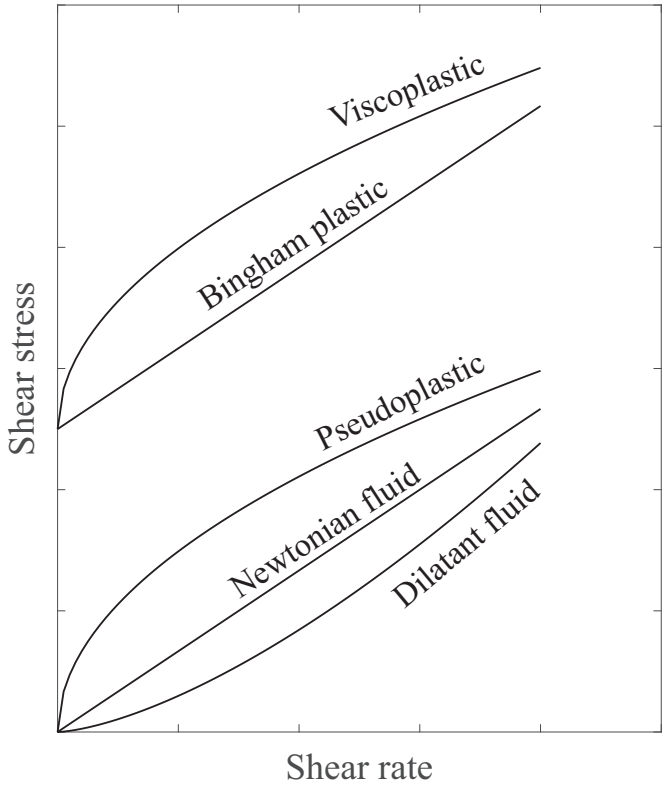


**Fig. 1.** Flow curves of different time independent fluids.

Fig. 1 visualizes Eq. (8) for different rheological media and makes evident that for Newtonian fluids the viscosity is a constant, independent of the shear rate, while non-Newtonian fluids may exhibit a viscosity changing with shear rate. Another difference may be the existence of a so-called yield stress, $\tau_0$, which must be exceeded for the fluid to deform or flow. Thus, although not strictly following the definition of a fluid, these materials behave like viscous fluids once the shear stress overcomes the yield stress, with flow curves being linear (Bingham plastic) or nonlinear (general viscoplastic).

There are rheological models to describe the different kinds of non-Newtonian fluids displayed in Fig. 1, such as the commonly used power-law model, the Bingham plastic model or the Casson model. Yet, the Herschel-Bulkley model [32] provides a flexible way to describe the different types of time-independent non-Newtonian fluids with a more general equation [33] and was shown to work well for the prediction of the rheology of particle suspensions [34]. The shear stress may then be modelled as

$$\begin{aligned} &\tau = \tau_0^H + k\dot{\gamma}^n && \tau > \tau_0^H \\ &\dot{\gamma} = 0 && \tau < \tau_0^H \end{aligned} \quad (9)$$

where $n$ is the flow-index and $k$ is the consistency index. The viscosity is then formulated as

$$\begin{aligned} &\mu = \tau_0^H \cdot \dot{\gamma}\, -1 + k \cdot \dot{\gamma}\, n-1 && \tau > \tau_0^H \\ &\mu = \infty && \tau < \tau_0^H \end{aligned} \quad (10)$$

For $n < 1$ the fluid exhibits a shear-thinning behavior (pseudoplastic), whereas for $n > 1$ the fluid is shear-thickening (dilatant). For $n = 1$ and $\tau_0 = 0$ the fluid is Newtonian.

Note, the Herschel-Bulkley yield stress, $\tau_0^H$ is not the true yield stress of the fluid, it is instead found by fitting the model to experimental data and extrapolating to zero shear rate. A granular system typically exhibits a non-Newtonian behavior, as shown by the work of Bagnold [35] or more recently by kinetic theory [23,36].

## 3. Method

### 3.1. Experimental setup

Falling-sphere-type experiments were conducted in a fluidized bed at $u_{mf}$ (considered homogeneous) at atmospheric pressure, doted with a high resolution tracking technique [24] to resolve the trajectory of the tracers used. Experiments were carried out in a cylindrical unit with an inner diameter of 0.074 m, in which spherical glass beads

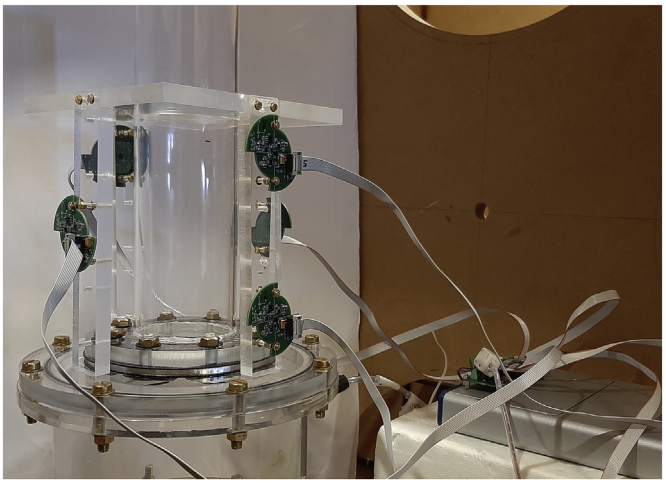

**Fig. 2.** Photo of the setup.

**Table 1**
Parameters of the fluidized bed used in the experiments.

| Parameter | Unit | |
|---|---|---|
| Bed diameter, $D_b$ | m | 0.074 |
| Bed material density, $\rho_s$ | kg/m$^3$ | 2600 |
| Bed material size, $d_s$ | $\mu$m | 212–250 |
| Bed height, $L_{mf}$ | m | 0.17 |
| Minimum fluid. velocity, $u_{mf}$ | m/s | 0.048 |
| Emulsion density, $\rho_{mf}$ | kg/m$^3$ | 1589 |

**Table 2**
Tracers.

| Name | Size [mm] | Weight [g] | Rel. density [kg/m$^3$] |
|---|---|---|---|
| $5_{-1}$ | 5.0 | 0.49 | −5898 |
| $8_{-1}$ | 8.0 | 2.03 | −5984 |
| $10_{-1}$ | 10.0 | 4.03 | −6108 |
| $10_{-4}$ | 10.0 | 2.32 | −2842 |
| $10_{-5}$ | 10.0 | 1.60 | −1467 |
| $20_{-1}$ | 20.0 | 32.05 | −6063 |
| $20_{-2}$ | 20.5 | 28.89 | −4816 |
| $20_{-3}$ | 20.0 | 20.34 | −3267 |
| $20_{-4}$ | 20.0 | 17.47 | −2582 |
| $20_{-5}$ | 20.0 | 13.37 | −1603 |
| $20_{+8}$ | 20.0 | 1.15 | +1314 |
| $20_{+9}$ | 20.0 | 1.66 | +1193 |
| $20_{+10}$ | 20.0 | 3.3 | +800 |

with a narrow size range of 212 to 250 $\mu$m and a solids density of 2600 kg/m$^3$ were fluidized with ambient air. The mass of the bed was about 1.1 kg, resulting in a static bed height of 0.16 m. Fig. 2 shows a photo of the rig setup. Note that the setup is made of polymethyl methacrylate (PMMA), which is known to cause electrostatic charges when fluidized with glass beads. However, as fluidization was mainly kept at minimum fluidization velocity, these effects were hardly observed and no countermeasures to ground the system were undertaken. To facilitate a smooth fluidization the gas passes through a high-pressure drop porous distributor plate before entering the bed. In this setup a minimum fluidization velocity of 0.048 m/s was obtained by observing the pressure signal with alternate sweeps of increasing and decreasing fluidization velocity. The key parameters that describe the fluidization system are summarized in Table 1.

Spherical tracers with four different diameters (5, 8, 10 and 20 mm) and with different densities (from negatively buoyant 5900 kg/m$^3$ to positively buoyant 800 kg/m$^3$) were used, see Table 2. The tracers consist of a commercial spherical NdFeB-based magnet with diameters ranging within 5–20 mm, which is either used directly or encapsulated in a plastic shield and filled with different non-magnetic materials to achieve the desired tracer density. Note, the density given in the table is the buoyant, i.e. the relative density of the tracer to the bed material. The bed used has an emulsion density of 1590 kg/m$^3$ at minimum fluidization. The tracers $20_{+8}$, $20_{+9}$ and $20_{+10}$, which have densities lower than the emulsion density are released from the bottom of the bed, from where they exhibit a rising trajectory. All other tracers are released from the bed surface, from where they sink into the bed and are therefore indicated with minus in Table 2.

A magnetic particle tracking system was use to follow the spheres immersed in the bed. A detailed description of the tracking principle and the configuration of the measurement system can be found in a previous work by the authors [24]. Only the improvements done on the system used for this work are shortly discussed here. The setup is equipped with five sensor assemblies consisting each of three anisotropic magneto resistance (AMR) sensors, which are placed around the bed (as seen in Fig. 2). By affecting the electrical resistance in the sensor element with the magnetic field of the tracer, the distance of the latter to each sensor can be calculated. By removing the external magnetic field, the sensor returns to its default magnetisation orientation. However, if the field is too strong the sensor becomes saturated and has to be reset by two electric pulses (S/R) that temporarily disable the sensor. While performed synchronously this procedure limited the sampling rate to 20 Hz. In the new system the sampling frequency of the tracking system has been enhanced by alternating the S/R pulses sent to one sensor at the time. With five sensors in place, there are always four elements measuring at the time, resulting in a maximum sampling frequency of 1.25 MHz/(3$N$), where $N$ is the number of sensor elements. The measurement data is filtered with a median filter yielding a final sample rate of 5 ms, which has been shown to preserve the core information in the trajectory and its time derivatives [24].

### 3.2. Experimental procedure

The measurements for each falling tracer are conducted according to the following procedure:

1. The bed is fluidized for at least 60 s at gas velocity of 0.085 m/s (bubbling conditions).
2. The fluidization is slowly reduced and set to 0.048 m/s (bubble free conditions, $u_{mf}$).
3. The tracer is released from the middle of the bed just above the bed surface.

For the rising tracer the procedure is slightly different:

1. The bed is fluidized for at least 60 s at 0.085 m/s (bubbling conditions).
2. The tracer is pushed down into bed and placed at the bottom with help of a thin thread.
3. The fluidization is set to 0.048 m/s and the air flow is closed with the main valve for 2 s to remove the thread.
4. The data acquisition is started and the fluidization is started by opening the main valve.

For each tracer the corresponding procedure is repeated ten times in order to ensure statistical robustness.

### 3.3. Data processing

The tracer trajectories obtained by the reconstruction algorithm are filtered using a moving average filter (window width of 8 points, i.e. 40 ms, for three times) to smooth the trajectories. In this way the non-physical local peaks of the acceleration values related to the detection system are removed. From the filtered trajectory data, velocity and acceleration data are obtained through time differentiation. Runs showing unstable trajectories (due to presence of bubbles, for instance) are discarded and not included in the data analysis reported in the results section.

According to the trajectory of the tracer inside the bed, the experiments can be classified in three groups: 1) the tracer falls all the way to the bottom, 2) the tracer falls but stagnates inside the bed or 3) the tracer rises from the bottom to the surface of the bed. Fig. 3 shows representative velocity profiles for these three cases which also exemplify the good repeatability. In the figure, the vertical location of the tracer (x-axis) is referred to a given reference location (close to the bottom distributor, the stagnation height, or the starting point for cases 1, 2 and 3, respectively).

For the falling cases, trajectories are evaluated from when the tracer is fully immersed in the bed, which corresponds to the moment it has reached its maximum velocity and starts to decelerate as the drag of the bed is dominating the motion of the tracer. For falling tracers reaching the bottom of the bed, trajectory data for locations too close to the bed bottom (<25mm) is discarded in order to disregard the bottom wall effect.

Note that for the case of stagnating falling tracers, although the tracer velocities when entering the bed are slightly different and the

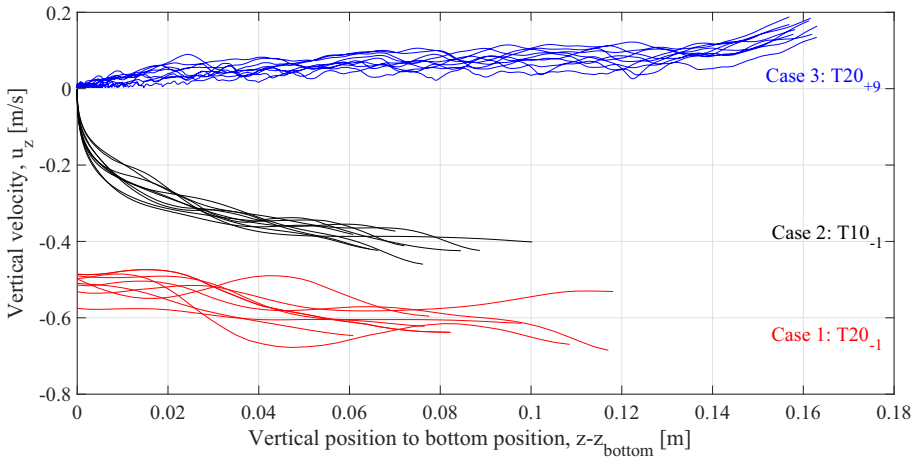


**Fig. 3.** Falling and rising velocities of the tracers against the tracer vertical location referred to a reference height (close to the bottom distributor, the stagnation height, or the starting point for cases 1, 2 and 3, respectively). Case 1: Tracer $20_{-1}$, falling to bottom (red), case 2: $10_{-1}$, stagnant (black) and case 3: $20_{+9}$, rising (blue).

tracers stagnate at different bed heights for each repetition, all curves follow a similar trajectory.

From Fig. 3 it can be seen that none of the tracers reaches a steady - terminal - velocity, instead they accelerate and/or decelerate while interacting with the bed.

After obtaining the velocity profiles, the comparison of the forces given in Eq. (4) is investigated to validate that the resistance of the fluidized bed against the heaviest tracer ($20_{-1}$) was large enough to be met by the measurement accuracy and frequency. The transient of the drag force obtained was at any point well-resolved, with a maximum of 0.405 N at a shear rate of 28.17 1/s, corresponding to a temporal resolution of 0.045 s (compared to the measurement resolution of 1/200 = 0.005 s).

For evaluation of the shear stress, the characteristic shear rate, $\frac{u_{rel}}{D_p}$, as suggested by Chhabra [33], is used. The velocity is here the relative velocity between the falling (or rising) tracer and the emulsion flow (cf. Eq. (2)).

## 4. Results and discussions

### 4.1. General observations of the shear stress

Fig. 4 shows the shear stress, $\tau$, over the characteristic shear rate, $\frac{u_{rel}}{D_p}$, for the repetitions of the falling and stagnating tracer $T10_{-1}$, calculated from the velocity data and by applying Eq. (7). Note, the time marching starts from the right-hand side of the figure and ends at zero shear rate. The shear stress of the tracer shows a clear offset at zero shear rate, which indicates a distinct yield stress, $\tau_0$. The stress has a relatively low dependence on the shear rate, but some trends can be observed. Starting from the yield stress at zero stress rate, the shear stress first increases non-linearly with shear rate, indicating a viscoplastic behavior. At higher slip velocities, which occur at the beginning of the trajectory of falling tracers, the stress first declines with stress rate and then eventually fluctuates around the same level as the yield stress, i.e. some instabilities can be observed.

All falling tracers show this qualitative pattern, with the quantitative influence of the tracer properties on the rheological behavior of the bed being studied hereafter. As the pattern explained above is not seen for the rising tracers, they are treated in a separate section.

Fig. 5 shows the shear stress, $\tau$, over the shear rate, $\frac{u_{rel}}{D_p}$ for a) 20 mm tracers with varying density, b) 10 mm tracers with varying density, and c) tracers with a relative density around 6000 kg/m$^3$ but varying size.

In Fig. 5a and b the yield stress increases with relative density, i.e. the density difference between the tracer and the bed emulsion. The variations of the shear stress with shear rate are stronger for tracers with higher density. Still, for all densities the contribution of the yield stress to the shear stress is higher than the contribution related to the shear rate. Since the heaviest tracer $20_{-1}$ rapidly reached the bottom of the bed, only the fluctuating part of its trajectory is displayed.

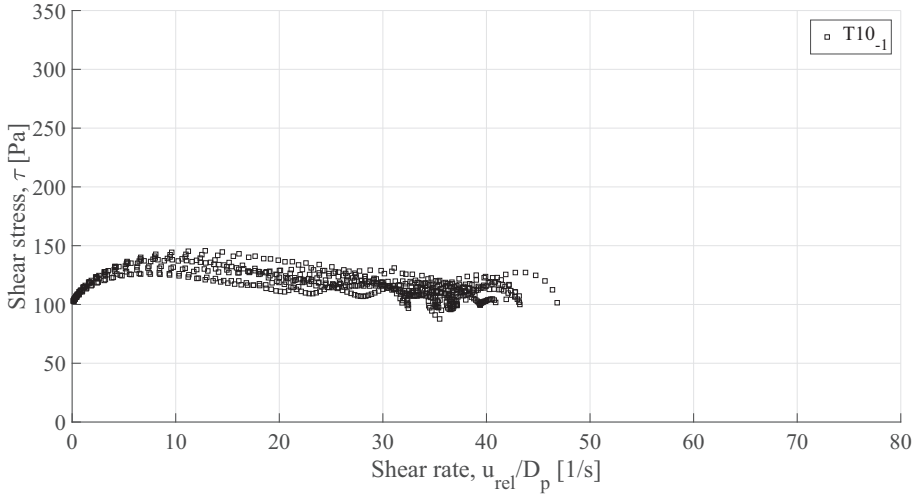


**Fig. 4.** Shear stress, $\tau$, vs. shear rate, $\frac{u_{rel}}{D_p}$. Typical curve for a falling tracer.

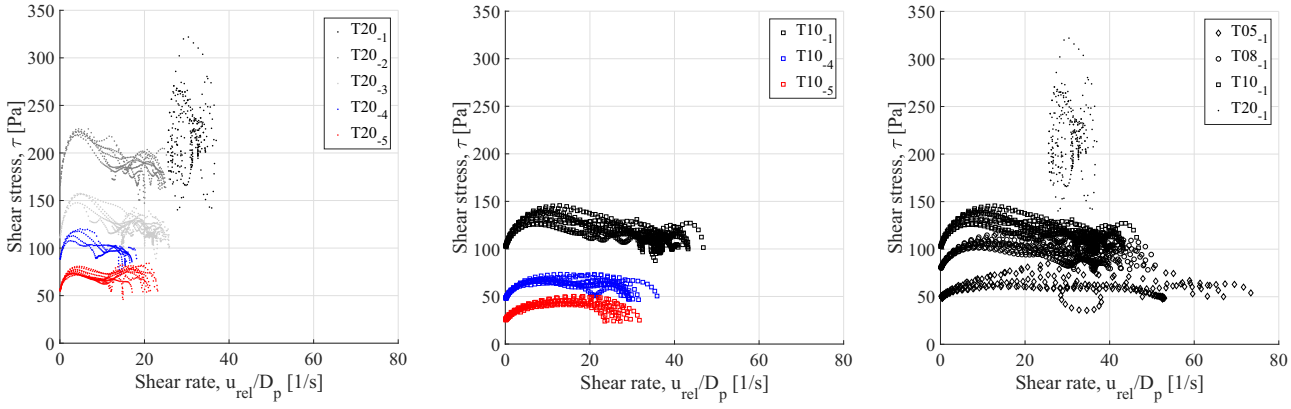


**Fig. 5.** Shear stress, $\tau$, vs. shear rate, $\frac{u_{rel}}{D_p}$. a) Shear stress of 20 mm tracers with different tracer densities. b) Shear stress of 10 mm tracers with different tracer densities. c) Shear stress of tracers with relative density around 6000 kg/m$^3$ and different tracer diameters.

When considering the effect of the tracer size, from comparing Fig. 5a and b and Fig. 5c it can be seen that both the yield stress and the contribution from the stress rate to the shear stress increase with tracer diameter. A larger diameter also causes the onset of the stress to decline and a fluctuating behavior at lower values of the shear rate. Larger tracers, entering the bed at higher Reynolds numbers, cause a stronger disturbance of the bed, which affects the local solid concentration of the latter, an results in stronger variations of the shear stress.

It should be noted, that for a given shear rate the shear stresses and yield stresses vary depending on relative density and size, which can be understood when studying Eq. (7). For a shear rate, i.e. tracer velocity, approaching stagnation the force balance (and thus the yield stress) reduces to the net gravitational term, which is therefore solely dependent on the relative density and size of the tracers and not on operational conditions. The correlation will be further discussed in Section 4.2.

At low shear rates, as the falling tracers have been decelerated by the bed emulsion and the intruders disturbance has been depleted, the shear stress exhibits viscoplastic behavior. The smaller the tracer, the less disturbance is caused in the bed, resulting in the viscoplastic region to cover a wider range of shear rates. For increasing shear rates the relationship is less clear: the shear stress decreases after reaching a maximum and fluctuates around the yield stress - trajectory data has shown that this corresponds to locations close to where the tracers have entered the bed. When intruding into the bed the tracer impacts the fluidized bed solids, the solids concentration increases locally, the bed is locally defluidized and bubbles may be released upon immersion of the tracer. Kolb et al. [37] discussed this influence of intruders on the local bed concentration and reported that for vertical intrusion through a solids bed a compacted area in front of the intruder and a cavity formed behind it. Thus, to only study the trajectory of a moving object in a homogeneous medium is not sufficient to explain the observed behavior. A vast number of authors have studied intruders entering water [38–41] and granular flows [37,42–45] and discussed the various phenomena occurring before the motion reaches stable conditions. Truscott et al. [39] discuss the importance of unsteady hydrodynamic forces on spheres during water entry, which are dominating for mass ratios $m^* = \rho_p/\rho_{em} < 8$. If applying this relation to the tracers and suspension used in this work, m* takes values between 2 and 5. The instabilities of the acceleration during impact and intrusion observed for the falling tracers in this work are similar to those reported by Goldman and Umbanhowar [43], who underlined the complex dynamics of intruders impacting granular media and also observed similar effects of the impact velocity, diameter and density of the spheres on the collision dynamics.

These effects on and from the local bed structure, as studied by the named literature, are difficult to assess from the data collected in the present work. However, complementary experiments using a higher bed and precise diagnostics of the local solids concentration by resolved capacitance or X-ray techniques could help revealing the details of the phenomena present in the entrance zone and the confirmation of local concentration fluctuations at the tracer entrance.

### 4.2. The yield gravity parameter

The dependency of the shear stress on the properties of the tracers as observed in Fig. 5a, b and c can be partly explained by the concept of a dimensionless group called the yield gravity parameter (see e.g. [33]). The yield gravity parameter is defined as the ratio of the forces due to yield stress and due to gravity

$$Y_0 = \frac{\tau_0}{gD_p\left(\rho_{em} - \rho_p\right)}. \tag{11}$$

The yield gravity parameter is typically used to discuss the static equilibrium of spherical objects in viscoplastic liquids as done by several authors [46–50], i.e. whether a sphere would move in an still viscoplastic. Although they evaluate the number for creeping flow with very slow and constant velocities, the relation becomes visible when studying Eq. (7).

Hence, for a steady velocity the right-hand-side reduces to the first term, which is based on the buoyancy of the tracer and is independent of the tracer motion. From this, the link to the definition of yield gravity parameter given by Eq. (11) above is made clear, and a normalized shear stress can be defined as

$$Y = \frac{\tau}{gD_p\left(\rho_{em} - \rho_p\right)}. \tag{12}$$

Fig. 6 plots, as a function of the shear rate, the normalized shear stress, defined in line with the concept of yield gravity, i.e. divided by the relative density, the diameter of each tracer and the gravitational acceleration. This results, as seen in Fig. 6, in normalized stress curves starting all in the same point for a zero stress rate, which for the falling and stagnating tracers in this work represents the static equilibrium of $Y_0 = 0.167$.

Using the concept of yield gravity, the shear stress data, obtained for all the falling tracers used in this work, can be generally described by fitting the Herschel-Bulkley model as presented in Eqs. (9) and (10) to

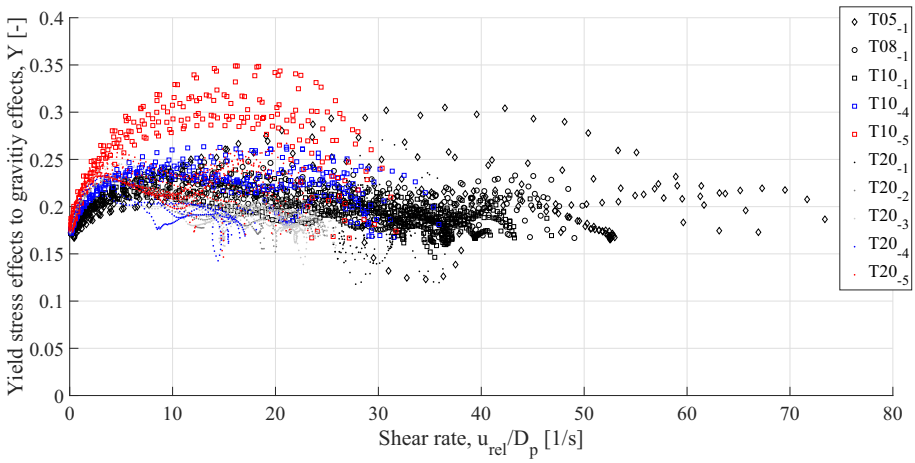


**Fig. 6.** Yield stress effects to gravity effects, $Y$ vs. shear rate, $\frac{u_{rel}}{D_p}$.

**Table 3**
Fitting result of falling tracers for $0<\frac{u_{rel}}{D_p}<5s^{-1}$.

| Parameter | Unit | |
|---|---|---|
| Yield gravity parameter, $Y_0$ | – | 0.167 |
| Consistency index, $k_0$ | $s^{-1}$ | 0.032 |
| Flow index, $n_0$ | – | 0.501 |

$$Y = 0.167 + 0.032\left(\frac{u_{rel}}{D_p}\right)^{0.501} \tag{13}$$

within the shear rate interval of $0<\frac{u_{rel}}{D_p}<5s^{-1}$. The fitting parameters are summarized in Table 3 revealing a consistency index of $k_0 = 0.033s^{-1}$ and a flow index of $n_0 = 0.486$. Fig. 7a shows the resulting fit and visualizes the viscoplastic behavior of the bed emulsion for the region of $0<\frac{u_{rel}}{D_p}<5s^{-1}$. With the obtained values a corresponding effective viscosity (normalized by gravity effects) can be calculated as plotted in Fig. 7b together with the measurement data.

Chhabra (2007) [33] discusses the various values of $Y_0$ in literature ranging from 0.04 — 0.08 for one group of measurements performed in liquids and ranging from 0.10 — 0.20 for measurements approaching the yield point from above, as it is done in this work and for which $Y_0 =$ 0.167 seems to agree reasonably well.

### 4.3. Rising tracers

In contrast to the falling tracers, the shear stress of the rising tracers fluctuate around the yield stress, $\tau_0$, with a rather constant low acceleration, i.e. although the rheological experience seems to be different the static equilibrium as characteristic for viscoplastics can be still be observed, Fig. 8a. The bed concentration seems to be effected less or the changes in the concentration have little influence on the rising movement of the tracers.

The different hydrodynamics of falling and rising objects observed in this work are in line with the experimental observations summarized by Chhabra [33] with spheres in pseudoplastic fluids. Note, pseudoplastic or shear-thinning fluids have similar flow numbers ($n < 1$) as viscoplastics, but exhibit no yield stress, cf. Fig. 1. Although there is no theoretical explanation, the authors attribute the difference in motion to an imbalance of the non-vertical forces on the spherical object, which arise from wake shedding behind the object. Chhabra found the hydrodynamics to differ in terms of drag-coefficient-Reynolds number relation, and the spiral motion clearly observed from the trajectories of rising tracers in this work was also reported by Chhabra. As observed in Fig. 8a, the shear-thinning behavior disappears and instead, the tracers are fluctuating around a constant yield stresses, which is also in line with the lack of shear-thinning behavior observed by Chhabra for creeping flows.

The normalized shear stress for rising tracers is plotted in Fig. 8b, revealing curves slightly fluctuating around the value of the yield gravity parameter obtained from the graph as $Y_0 = 0.167$, as expected from Eq. (7).

### 4.4. Influence of the gas drag

The contribution of the gas drag can investigated by studying the motion of the rising tracers, which experience much lower forces than the falling tracers. The drag of the gas on the tracer particle can be estimated with Eq. (6) by using the drag coefficient of the gas, $C_{Dg}$, the relative velocity of the gas to the tracer, $\left(\frac{u_0}{\varepsilon_{mf}} - u_z\right)$, and the effective gas density, $(\varepsilon_{mf}\rho_g)$, with the voidage, $\varepsilon_{mf}$, obtained from Eq. (3). The average and standard deviation of each force acting on the tracer for each run is calculated and/or extracted from trajectory data and given by Table 4, which displays the averages for the 10 runs with each tracer. As seen, the buoyancy and drag forces exerted by the bed emulsion are dominating and balancing each other, while the added mass and gas drag forces are two and four orders of magnitude smaller, respectively. This confirms the gas drag can be neglected.

## 5. Conclusion

This work presents experimental work on falling and rising solid spheres in a gas-solids fluidized bed at minimum fluidization, using unique highly resolved tracer trajectories obtained by magnetic particle tracking.

The trajectories show clearly that no terminal velocity (either rising or falling) is reached for any of the tracers, while moving through the 16-cm tall bed. Instead, the tracers show vigorous interaction with the bed emulsion, resulting in a fluctuating acceleration behavior. For all tracers tested, the yield stress is larger than the contribution of the shear stress within the window of shear stress rate tested here ($\frac{u_{rel}}{D_p}<75s^{-1}$). It can be seen that stress fluctuations increase with tracer size and relative density, and so does the yield stress.

For falling tracers, at the region close to the entrance of the tracer into the bed, the shear stress is highly affected by the impacting tracer disturbing the bed; local defluidization and bubble release may occur, possibly resulting in local changes of the solids concentration. Except for the heaviest tracer, the falling tracers get decelerated and stagnate before reaching the bottom plate. This behavior is similar for all falling

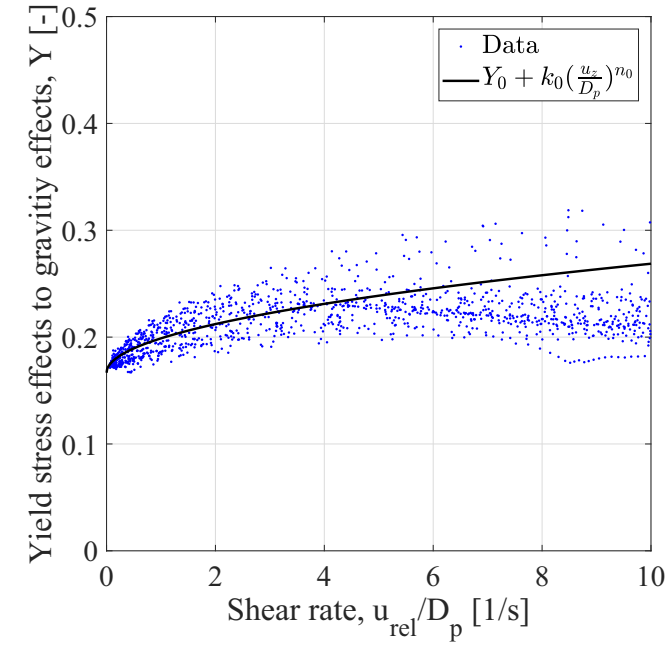


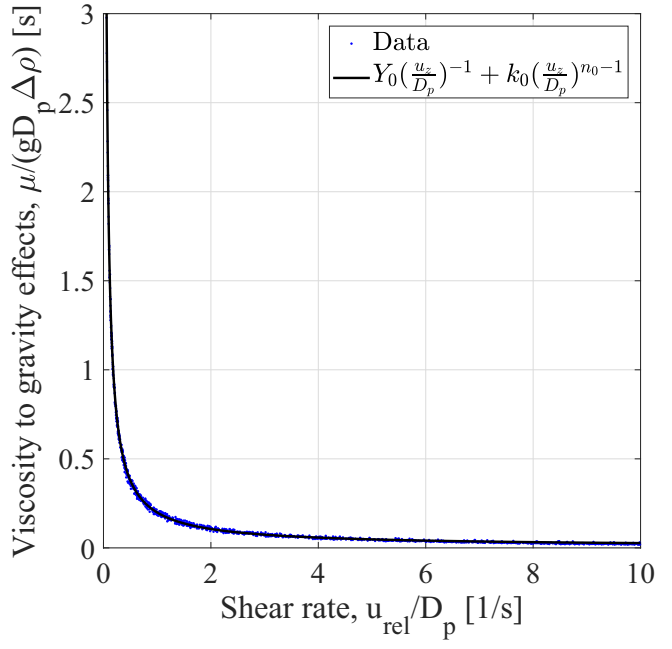


**Fig. 7.** Fitting of a) the Yield stress effects to gravity effects, *Y* and b) the viscosity to gravity effects vs. shear rate, $\frac{u_{rel}}{D_p}$.

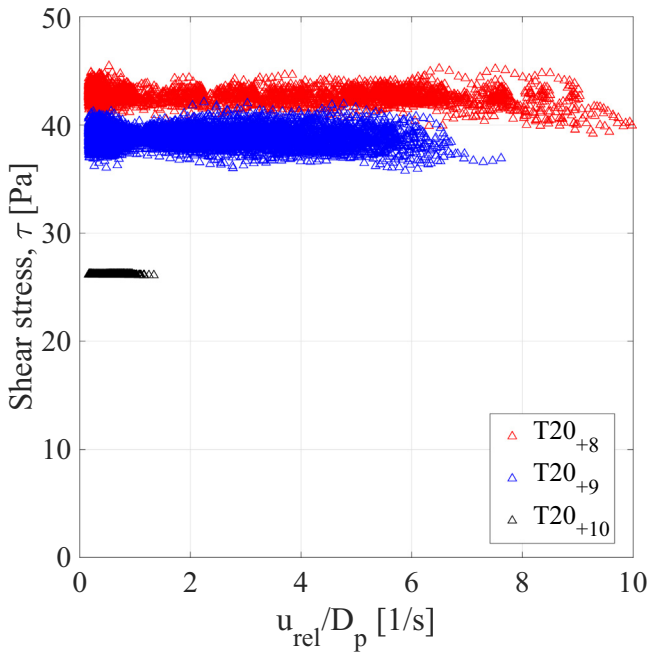


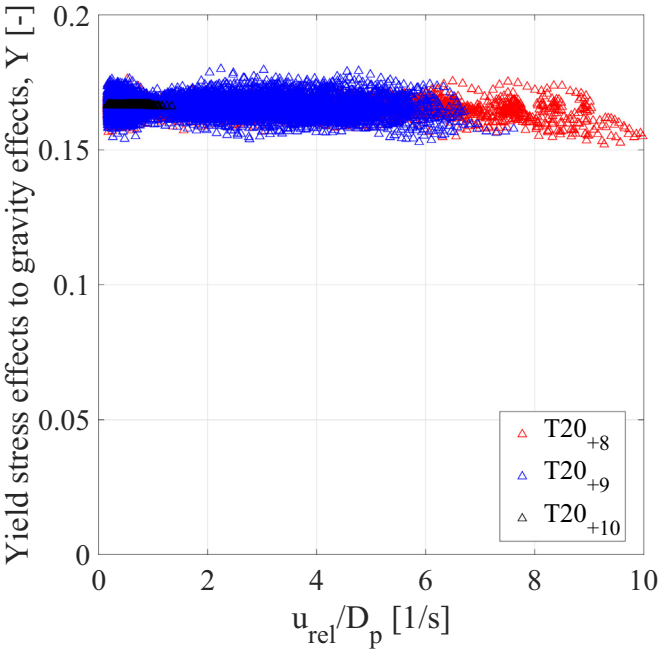


**Fig. 8.** a) Shear stress, $\tau$, vs. shear rate, $\frac{u_{rel}}{D_p}$ of the rising tracers. b) Yield stress effects to gravity effects, *Y* vs. shear rate, $\frac{u_{rel}}{D_p}$ of the rising tracers.

tracers and reveals a viscoplastic behavior at low shear rates before reaching static equilibrium. By normalizing the shear stress with the relative density, the diameter of each tracer and the gravitational acceleration, this behavior could be described. The date fits well the Herschel-Bulkley model, reading

$$Y = \frac{\tau}{gD_p\left(\rho_{em}-\rho_p\right)} = 0.167 + 0.032\left(\frac{u_{rel}}{D_p}\right)^{0.501}$$

in the shear rate interval of $0 < \frac{u_{rel}}{D_p} < 5s^{-1}$.

For the rising tracers, the shear stress shows little dependency on the shear rate over the stress rate investigated ($\frac{u_{rel}}{D_p} < 10s^{-1}$) and thus can be approached with the yield stress.

**Table 4**
Forces acting on rising tracers.

| Tracer | | $20_{+8}$ | $20_{+9}$ | $20_{+10}$ |
|---|---|---|---|---|
| Buoyancy, $F_B$ [N] | Avg | 0.0486 | 0.0490 | 0.0329 |
| | Std | 0.0 | 0.0 | 0.0 |
| Emulsion drag, $F_{D,\,em}$ [N] | Avg | 0.0482 | 0.0488 | 0.0329 |
| | Std | 0.0010 | 0.0011 | 0.30e-04 |
| Added mass, $F_{add}$ [N] | Avg | 3.04e-04 | 1.57e-04 | 0.08e-04 |
| | Std | 7.46e-04 | 7.01e-04 | 0.15e-04 |
| Gas drag, $F_{D,\,g}$ [N] | Avg | 0.01e-04 | 0.02e-04 | 0.01e-04 |
| | Std | 0.04e-04 | 0.04e-04 | 0.00e-04 |

Studying the influence of the gas drag on the tracers showed that the gas drag is estimated to have a negligible effect on the tracers motion.

## Declaration of Competing Interest

The authors declare that they have no known competing financial interests or personal relationships that could have appeared to influence the work reported in this paper.

## Acknowledgement

The research leading to this work was financed by the Swedish Gasification Centre (SFC) within the framework of the Centre for Indirect Gasification of Biomass (CIGB) and by the Swedish Energy Agency within the framework of project P-38347-2.

## References

[1] A. Einstein, Eine neue Bestimmung der Moleküldimensionen, Ann. Phys. 324 (2) (1906) 289–306, https://doi.org/10.1002/andp.19063240204.
[2] I.R. Rutgers, Relative viscosity of suspensions of rigid spheres in Newtonian liquids, Rheol. Acta 2 (3) (1962) 202–210, https://doi.org/10.1007/BF01983952.
[3] D.G. Thomas, Transport characteristics of suspension: VIII. A note on the viscosity of Newtonian suspensions of uniform spherical particles, J. Colloid Sci. 20 (3) (1965) 267–277, https://doi.org/10.1016/0095-8522(65)90016-4.
[4] G.K. Batchelor, J.T. Green, The determination of the bulk stress in a suspension of spherical particles to order c2, J. Fluid Mech. 56 (3) (1972) 401–427, https://doi.org/10.1017/S0022112072002435.
[5] M. Poletto, D.D. Joseph, Effective density and viscosity of a suspension, J. Rheol. 39 (2) (1995) 323–343, https://doi.org/10.1122/1.550692.
[6] R. Di Felice, P.U. Foscolo, L.G. Gibilaro, S. Rapagna, The interaction of particles with a fluid—particle pseudo—fluid, Chem. Eng. Sci. 46 (7) (1991) 1873–1877, https://doi.org/10.1016/0009-2509(91)87035-B.
[7] R. Di Felice, P. Pagliai, The falling velocity of a large sphere in a suspension of smaller spheres, Int. J. Multiphase Flow 33 (7) (2007) 797–801, https://doi.org/10.1016/j.ijmultiphaseflow.2007.01.002.
[8] L.G. Gibilaro, K. Gallucci, R. Di Felice, P. Pagliai, On the apparent viscosity of a fluidized bed, Chem. Eng. Sci. 62 (1–2) (2007) 294–300, https://doi.org/10.1016/j.ces.2006.08.030.
[9] T.C. Daniels, Density separation in gaseous fluidized beds, Rheol. Disperse Syst. 5 (1959) 211–221.
[10] D.F. King, F.R.G. Mitchell, D. Harrison, Dense phase viscosities of fluidised beds at elevated pressures, Powder Technol. 28 (1) (1981) 55–58, https://doi.org/10.1016/0032-5910(81)87009-X.
[11] T. Kai, M. Murakami, K. Ichi Yamasaki, T. Takahashi, Relationship between apparent bed viscosity and fluidization quality in a fluidized bed with fine particles, J. Chem. Eng. Japan 24 (4) (1991) 494–500, https://doi.org/10.1252/jcej.24.494.
[12] T.C. Daniels, Measurement of the drag on spheres moving through gaseous fluidized beds, J. Mech. Eng. Sci. 4 (2) (1962) 103–110, https://doi.org/10.1243/JMES_JOUR.1962.004.016.02.
[13] T.C. Daniels, Measurement of the drag on immersed bodies in fluidised beds, Rheol. Acta 4 (3) (1965) 192–197, https://doi.org/10.1007/BF01969255.
[14] L. Wei, Q. Chen, Calculation of drag force on an object settling in gas-solid fluidized beds, Part. Sci. Technol. 19 (3) (2001) 229–238, https://doi.org/10.1080/02726350290057822.
[15] A.C. Rees, J.F. Davidson, J.S. Dennis, A.N. Hayhurst, The apparent viscosity of the particulate phase of bubbling gas-fluidized beds: a comparison of the falling or rising sphere technique with other methods, Chem. Eng. Res. Des. 85 (10) (2007) 1341–1347, https://doi.org/10.1016/S0263-8762(07)73173-8.
[16] K. Schügerl, M. Merz, F. Fetting, Rheologische eigenschaften von gasdurchströmten fliessbettsystemen, Chem. Eng. Sci. 15 (1–2) (1961) 1–38, https://doi.org/10.1016/0009-2509(61)85001-X.
[17] P. Anjaneyulu, D.V. Khakhar, Rheology of a gas-fluidized bed, Powder Technol. 83 (1995) 29–34.
[18] A. Colafigli, L. Mazzei, P. Lettieri, L. Gibilaro, Apparent viscosity measurements in a homogeneous gas-fluidized bed, Chem. Eng. Sci. 64 (1) (2009) 144–152, https://doi.org/10.1016/j.ces.2008.08.036.
[19] B. Lv, Y. Fu, Z. Luo, B. Zhang, X. Qin, X. Zhu, Viscosity and separation performance of a gas-solid separation fluidized beds, Adv. Powder Technol. 29 (12) (2018) 3375–3384, https://doi.org/10.1016/j.apt.2018.09.017.
[20] S. Chen, R. Cai, Y. Zhang, H. Yang, H. Zhang, J. Lyu, A semi-empirical model to estimate the apparent viscosity of dense, bubbling gas-solid suspension, Powder Technol. 377 (2021) 289–296, https://doi.org/10.1016/j.powtec.2020.08.089.
[21] J.R. Grace, The viscosity of fluidized beds, Can. J. Chem. Eng. 48 (1) (1970) 30–33, https://doi.org/10.1002/cjce.5450480106.
[22] G. Van Den Langenberg-Schenk, K. Rietema, The rheology of homogeneously gas-fluidized solids, studied in a vertical standpipe, Powder Technol. 38 (1) (1984) 23–32, https://doi.org/10.1016/0032-5910(84)80030-3.
[23] K. Wu, V. Francia, M.-O. Coppens, Dynamic viscoplastic granular flows: a persistent challenge in gas-solid fluidization, Powder Technol. 365 (2020) 172–185, https://doi.org/10.1016/j.powtec.2019.04.053.
[24] A. Köhler, D. Pallarès, F. Johnsson, Magnetic tracking of a fuel particle in a fluid-dynamically down-scaled fluidised bed, Fuel Process. Technol. 162 (2017) 147–156, https://doi.org/10.1016/j.fuproc.2017.03.018.
[25] T.R. Auton, J.C.R. Hunt, M. Prud'Homme, The force exerted on a body in inviscid unsteady non-uniform rotational flow, J. Fluid Mech. 197 (1988) 241–257, https://doi.org/10.1017/S0022112088003246.
[26] R.H. Perry, D.W. Green, J.O. Maloney, Perry's chemical engineers' handbook, Book, Whole, 7th ed.McGraw-Hill, New York, 1997.
[27] A.R. Khan, J.F. Richardson, Fluid-particle interactions and flow characteristics of fluidized beds and settling suspensions of spherical particles, Chem. Eng. Commun. 78 (1) (1989) 111–130, https://doi.org/10.1080/00986448908940189.
[28] T.Z. Harmathy, Velocity of large drops and bubbles in media of infinite or restricted extent, AICHE J. 6 (2) (1960) 281–288, https://doi.org/10.1002/aic.690060222.
[29] U. Andres, Equilibrium and motion of spheres in a viscoplastic liquid, Sov. Phys. Dokl. (U.S.A.) 5 (1960) 723.
[30] X. Tian, J. Yang, Z. Guo, Q. Wang, B. Sunden, Numerical study of heat transfer in gravity-driven dense particle flow around a hexagonal tube, Powder Technol. 367 (2020) 285–295, https://doi.org/10.1016/j.powtec.2020.04.001 , URL https://www.sciencedirect.com/science/article/pii/S0032591020302849.
[31] A.C. Rees, J.F. Davidson, J.S. Dennis, A.N. Hayhurst, The rise of a buoyant sphere in a gas-fluidized bed, Chem. Eng. Sci. 60 (4) (2005) 1143–1153, https://doi.org/10.1016/j.ces.2004.09.045.
[32] W.H. Herschel, R. Bulkley, Konsistenzmessungen von Gummi-Benzollösungen, Kolloid-Zeitschrift 39 (4) (1926) 291–300, https://doi.org/10.1007/BF01432034.
[33] R.P. Chhabra, Bubbles, Drops, and Particles in Non-Newtonian Fluids, CRC Press, 2007https://doi.org/10.1201/9781420015386.
[34] S. Mueller, E.W. Llewellin, H.M. Mader, The rheology of suspensions of solid particles, Proc. Royal Soc. A: Math. Phys. Eng. Sci. 466 (2116) (2010) 1201–1228, https://doi.org/10.1098/rspa.2009.0445.
[35] R.A. Bagnold, Experiments on a gravity-free dispersion of large solid spheres in a Newtonian fluid under shear, Proc. Royal Soc. Lond. Ser. A. Math. Phys. Sci. 225 (1160) (1954) 49–63, https://doi.org/10.1098/rspa.1954.0186.
[36] J.T. JENKINS, D.M. HANES, Collisional sheet flows of sediment driven by a turbulent fluid, J. Fluid Mech. 370 (1998) 29–52, https://doi.org/10.1017/S0022112098001840.
[37] E. Kolb, P. Cixous, N. Gaudouen, T. Darnige, Rigid intruder inside a two-dimensional dense granular flow: drag force and cavity formation, Phys. Rev. E Stat. Nonlinear Soft Matter Phys. 87 (3) (2013) 1–9, https://doi.org/10.1103/PhysRevE.87.032207.
[38] A. May, J.C. Woodhull, Drag coefficients of steel spheres entering water vertically, J. Appl. Phys. 19 (12) (1948) 1109–1121, https://doi.org/10.1063/1.1715027.
[39] T.T. Truscott, B.P. Epps, A.H. Techet, Unsteady forces on spheres during free-surface water entry, J. Fluid Mech. 704 (2012) 173–210, https://doi.org/10.1017/jfm.2012.232.
[40] T. Shepard, J.P. Abraham, D. Schwalbach, S. Kane, D. Siglin, T. Harrington, Velocity and density effect on impact force during water entry of sphere, J. Geophys. Rem. Sens. 03 (03) (2014)https://doi.org/10.4172/2169-0049.1000129.
[41] J.M. Gorman, J.P. Abraham, D. Schwalbach, T. Shepard, J. Stark, F. Reseghetti, Experimental verification of drag forces on spherical objects entering water, J. Mar. Biol. Oceanogr. 03 (2) (2014)https://doi.org/10.4172/2324-8661.1000126.
[42] R. Bharadwaj, C. Wassgren, R. Zenit, The unsteady drag force on a cylinder immersed in a dilute granular flow, Phys. Fluids 18 (4) (2006)https://doi.org/10.1063/1.2191907.
[43] D.I. Goldman, P. Umbanhowar, Scaling and dynamics of sphere and disk impact into granular media, Phys. Rev. E Stat. Nonlinear Soft Matter Phys. 77 (2) (2008) 1–14 , arXiv:0709.4043 https://doi.org/10.1103/PhysRevE.77.021308.
[44] H. Zheng, D. Wang, D.Z. Chen, M. Wang, R.P. Behringer, Intruder friction effects on granular impact dynamics, Phys. Rev. E 98 (3) (2018) 1–5, https://doi.org/10.1103/PhysRevE.98.032904.
[45] L. Jing, J.M. Ottino, R.M. Lueptow, P.B. Umbanhowar, Rising and sinking intruders in dense granular flows, Phys. Rev. Res. 2 (2) (2019) 22069, https://doi.org/10.1103/PhysRevResearch.2.022069.
[46] J. Schurz, The yield stress — an empirical reality, Rheol. Acta 29 (2) (1990) 170–171, https://doi.org/10.1007/BF01332384.
[47] D.D. Atapattu, R.P. Chhabra, P.H.T. Uhlherr, Creeping sphere motion in Herschel-Bulkley fluids: flow field and drag, J. Non-Newtonian Fluid Mech. 59 (2) (1995) 245–265, https://doi.org/10.1016/0377-0257(95)01373-4.
[48] M. Beaulne, E. Mitsoulis, Creeping motion of a sphere in tubes filled with Herschel-Bulkley fluids, J. Non-Newtonian Fluid Mech. 72 (1) (1997) 55–71, https://doi.org/10.1016/S0377-0257(97)00024-4.
[49] L. Jossic, A. Magnin, Drag and stability of objects in a yield stress fluid, AICHE J. 47 (12) (2001) 2666–2672, https://doi.org/10.1002/aic.690471206.
[50] O. Merkak, L. Jossic, A. Magnin, Spheres and interactions between spheres moving at very low velocities in a yield stress fluid, J. Non-Newtonian Fluid Mech. 133 (2) (2006) 99–108, https://doi.org/10.1016/j.jnnfm.2005.10.012.